Precession and atmospheric CO_2 modulated variability of sea ice in the central Okhotsk Sea since 130,000 years ago

Li Lo[a,b,*], Simon T. Belt[c], Julie Lattaud[d], Tobias Friedrich[e], Christian Zeeden[f], Stefan Schouten[d,g], Lukas Smik[c], Axel Timmermann[e,h], Patricia Cabedo-Sanz[c], Jyh-Jaan Huang[i,#], Liping Zhou[j], Tsong-Hua Ou[k], Yuan-Ping Chang[l], Liang-Chi Wang[m], Yu-Min Chou[n], Chuan-Chou Shen[i], Min-Te Chen[o], Kuo-Yen Wei[i], Sheng-Rong Song[i], Tien-Hsi Fang[o], Sergey A. Gorbarenko[p], Wei-Lung Wang[q], Teh-Quei Lee[r], Henry Elderfield[b,†], David A. Hodell[b]

[a] State Key Laboratory of Isotope Geochemistry, Guangzhou Institute of Geochemistry, Chinese Academy of Sciences, Guangzhou 510640, China.
[b] Godwin Laboratory for Palaeoclimate Research, Department of Earth Sciences, University of Cambridge, Downing Street, Cambridge CB2 3EQ, UK.
[c] Biogeochemical Research Centre, School of Geography, Earth and Environmental Sciences, Plymouth University, Plymouth PL4 8AA, UK.
[d] NIOZ, Royal Netherlands Institute for Sea Research, Department of Marine Microbiology and Biogeochemistry, and Utrecht University, PO Box 59, 1790 AB Den Burg, The Netherlands.
[e] International Pacific Research Center, School of Ocean and Earth Science and Technology, University of Hawaii at Monoa, Honolulu, Hawaii 96822, USA.
[f] IMCCE, Observatoire de Paris, PSL Research University, CNRS, Sorbonne Universités, UPMC Univ Paris 06, Univ Lille, 75014 Paris, France.
[g] Faculty of Geosciences, Department of Earth Sciences, Utrecht University, PO Box 80.021, 3508 TA, The Netherlands.
[h] Institute of Basic Science, Center for Climate Physics, Pusan National University, Busan 46241, Republic of Korea.
[i] Department of Geosciences, National Taiwan University, Taipei 10617, Taiwan ROC.
[j] Laboratory for Earth Surface Processes, Department of Geography, and Institute of Ocean Research, Peking University, Beijing 100871, China.
[k] Institute of Applied Mechanics, National Taiwan University, Taipei 10617, Taiwan ROC.
[l] Department of Oceanography, National Sun Yat-sen University, Kaohsiung 80424, Taiwan ROC.
[m] Collection Management Department, National Taiwan Museum, Taipei 10046, Taiwan ROC.
[n] Department of Ocean Science and Engineering, Southern University of Science and Technology, Shenzhen, Gongdong 518055, China.
[o] Institute of Applied Geosciences, National Taiwan Ocean University, Keelung 20224, Taiwan ROC.
[p] V.I. Il'ichev Pacific Oceanological Institute, Far East Branch Russian Academy of Science, Vladivostok 690041, Russia.
[q] Department of Biology, National Changhua University of Education, Changhua 50074, Taiwan ROC.
[r] Institute of Earth Sciences, Academia Sinica, Taipei 11529, Taiwan ROC.

[*]To whom correspondence should be addressed
Email address: lilo@gig.ac.cn (Li Lo)

[#]now at Institute of Geology, University of Innsbruck, Innrain 52, A-6020, Innsbruck, Austria

[†] Deceased

Revised and resubmitted to *Earth and Planetary Science Letters*
January 30, 2018

ABSTRACT

Recent reduction in high-latitude sea ice extent demonstrates that sea ice is highly sensitive to external and internal radiative forcings. In order to better understand sea ice system responses to external orbital forcing and internal oscillations on orbital timescales, here we reconstruct changes in sea ice extent and summer sea surface temperature (SSST) over the past 130,000 years in the central Okhotsk Sea. We applied novel organic geochemical proxies of sea ice (IP_{25}), SSST (TEX^{L}_{86}) and open water marine productivity (a tri-unsaturated highly branched isoprenoid and biogenic opal) to marine sediment core MD01-2414 (53°11.77'N, 149°34.80'E, water depth 1123 m). To complement the proxy data, we also carried out transient Earth system model simulations and sensitivity tests to identify contributions of different climatic forcing factors. Our results show that the central Okhotsk Sea was ice-free during Marine Isotope Stage (MIS) 5e and the early-mid Holocene, but experienced variable sea ice cover during MIS 2-4, consistent with intervals of relatively high and low SSST, respectively. Our data also show that the sea ice extent was governed by precession-dominated insolation changes during intervals of atmospheric CO_2 concentrations ranging from 190 to 260 ppm. However, the proxy record and the model simulation data show that the central Okhotsk Sea was near ice-free regardless of insolation forcing throughout the penultimate interglacial, and during the Holocene, when atmospheric CO_2 was above ~260 ppm. Past sea ice conditions in the central Okhotsk Sea were therefore strongly modulated by both orbital-driven insolation and CO_2-induced radiative forcing during the past glacial/interglacial cycle.

Keywords: Okhotsk Sea, Sea ice, Insolation, Greenhouse gases, Precession cycle

Highlights:

1. The first orbital timescale proxy-model sea ice-sea surface temperature records from the northwestern subarctic Pacific Ocean.
2. Strong precession forcing controlled sea ice variations are modulated by greenhouse gas radiative forcing.
3. Sea ice remained free in the central Okhotsk Sea during MIS 5e due to high greenhouse gas radiative forcing.

1. Introduction

Sea ice is one of the crucial components of the Earth's climate system, in part, due to its high reflectance or albedo, which influences energy budgets at both high and low latitudes (Serreze et al., 2016; Turner et al., 2016). In addition, brine rejection during seasonal sea ice formation supplies dense and well ventilated water to global deep/intermediate water circulation, while sea ice melt in spring causes stratification between near-surface and deeper water masses. Furthermore, the area bound by the retreating sea ice margin during spring and summer (the so-called marginal ice zone) represents a region of significant open water (pelagic) productivity.

Major changes in the extent and thickness of sea ice across the Arctic-subarctic and Antarctic regions during the last three to four decades have been revealed by direct and remote sensing observations (Serreze et al., 2016; Turner et al., 2016). In the Arctic, the average reduction rate in September sea ice extent, 13.4% per decade during 1981-2010, is higher than predicted by most model simulations (Serreze et al., 2016). This discrepancy emphasizes the limited knowledge of the high-latitude climate system to radiative perturbations and natural variability. In addition, a slow overall increase in annual mean sea ice extent in the Southern Ocean (ca. 1.6% per decade during 1979-2013), raises further questions regarding the relationships between anthropogenic radiative forcings, temperature, winds, and sea ice cover (Turner et al., 2016).

The Okhotsk Sea in the subarctic Pacific Ocean has responded rapidly to recent climate change (Mesquita et al., 2011; Kashiwase et al., 2014) and has been shown previously to be dynamically connected to Northern Hemispheric cooling events (e.g. Heinrich and Dansgaard–Oeschger (D/O) events) during the last glacial period (Ono et al., 2005; Sakamoto et al., 2005; Harada et al., 2008; Max et al., 2012; 2014). For example, Harada et al. (2008) demonstrated a strong link between a $U^{K'}_{37}$-derived sea surface temperature (SST) record and Greenland Ice Sheet Project 2 ice core D/O events back to ~120 ka in the southwestern Okhotsk Sea. Further, sedimentary magnetic mineral and composition data have been used to reconstruct sea ice derived ice rafted debris (IRD) in the same region (Sakamoto et al., 2005) with larger fluctuations during last glacial period (Marine Isotope Stage, MIS 2-4) compared to interglacial periods (Holocene and MIS 5) for the southwestern Okhotsk Sea. Also within the study region, freshwater input from the Amur River and polar atmospheric dynamics are potential candidates responsible for controlling sea ice dynamics in the southwestern Okhotsk Sea (Sakamoto et al., 2005; Harada et al., 2008). Previous low resolution sea ice reconstructions based on the Arctic sea ice biomarker proxy IP_{25} (Ice Proxy with 25 carbon atoms, Belt et al., 2007; Belt and Müller, 2013), when combined with compiled SST data, have shown that sea ice extent variations in the central-west subarctic Pacific Ocean are tightly link to Atlantic meridional overturning circulation and atmospheric circulation between North Atlantic and North Pacific during the last termination (Max et al. 2012; 2014). More recently, Méheust et al. (2016) used IP_{25} and other geochemical proxies to show that sea ice expanded significantly during Heinrich event 1 (H1) and the Younger Dryas (YD) in the western Bering Sea, in contrast to the Bølling-Allerød (B/A) and early Holocene, which experienced low/absent sea ice.

Despite the importance of its location and role in the subarctic sea ice system, very few studies have been reported from the central region of the Okhotsk Sea (Liu et al., 2006; Wang and Wang, 2008; Chou et al., 2011) and no detailed sea ice reconstructions have been conducted on orbital timescales. As such, the roles of insolation (external) and greenhouse gas radiative forcing (internal) on sea ice variation remain poorly understood. Therefore, long-term reconstruction of sea ice extent in the central Okhotsk Sea would be especially informative in understanding the interaction of sea ice and external/internal climatic forcings.

In this study, we reconstruct variations in sea ice extent and summer SST (SSST) using organic geochemical proxies and compare the proxy-derived records with Earth system modelling results in order to identify controlling mechanisms and interactions between sea ice and atmospheric-oceanic forcings in the Okhotsk Sea during the past 130,000 years. Our results reveal a strong precession control and a potential greenhouse gas induced radiative forcing threshold on sea ice variations since the penultimate peak interglacial period.

2. Regional setting

The Okhotsk Sea represents the southernmost region of contemporary seasonal sea ice formation in the Northern Hemisphere and has experienced a large decline rate of 11.4% per decade in sea ice extent during the past three decades (Kashiwase et al., 2014). The regional current system is affected by the north- and south-ward flowing

West Kamchatka Current (WKC), East Sakhalin Current (ESC), salty-warm Soya Warm Current (SWC) and freshwater input from the Amur River (Fig. 1). The SSST is in the range 5–13°C, while salinity varies between 31.5 to 33.2‰, being influenced mostly by the Amur River discharge (Luchin et al., 2009). Sea ice easily forms on the shallow continental shelves in the north-west Okhotsk Sea and is also influenced by the large fresh water input by the Amur River. As a result, the Okhotsk Sea is the southernmost region of subarctic sea ice distribution in the world (Kimura and Wakatsuchi, 2004; Nishioka et al., 2014).

3. Material and methods

3.1 Sediment core MD01-2414 and surface sediments

Marine sediment core MD01-2414 (53°11.77'N, 149°34.80'E, water depth 1123 m, total sediment length 52.76 m, Chou et al., 2011, Supplementary Fig. 1) was drilled from the Deryugin Basin during the circum-Pacific initiative cruise in 2001 as part of the IMAGES project (Fig. 1). The upper 235-cm segment was not suitable for XRF scanning due to its high water content (Liu et al., 2006). The main sediment composition is terrestrial detritus (from sand to silty clay) with diatom and rare calcareous (nannofossil and foraminifera) oozes (Liu et al., 2006; Wang and Wang, 2008; Chou et al., 2011). The ash layers and core gaps resulting from the coring process were eliminated to prevent bias when performing sedimentation rate calculations (Chou et al., 2011). In this study, we used sediment of the upper 700 cm to generate sea ice and SSST histories covering the past 130,000-yrs. To complement the long-term records, we also examined biomarker content in a number of surface sediments from the region (Supplementary Fig. 2, Supplementary Table 3).

3.2 Sediment core XRF scanning

Non-destructive X-ray fluorescence (XRF) scanning was performed by the ITRAX @ COX company. Continuous downcore measurements of elemental variations were done in the ITRAX-XRF Core Scanner Laboratory, Department of Geosciences, National Taiwan University (Huang et al., 2016). A U-channel of core MD01-2414 was scanned using the 3 kW Mo source. The XRF measurements were analyzed at 30 kV, 24 mA, 2 mm resolution with a 30 second exposure time. The original XRF spectra were processed by the Q-Spec software provided by COX Analytical Systems to obtain element peak areas in counts.

3.3 Age model

The MD01-2414 age model was established based on accelerator mass spectrometry radiocarbon (AMS ^{14}C) dates and XRF data correlation to the global composite benthic foraminiferal oxygen isotope curve (LR04, Fig. 3H; Lisiecki and Raymo, 2005). Samples of the planktonic foraminifera *Neogloboquadrina pachyderma* (>125 μm, *sinistral*) were picked from five depths (33, 113, 143, 170, and 210 cm). AMS ^{14}C dates were obtained by the College of Urban and Environmental Sciences, Peking University. AMS ^{14}C dates were calibrated to calendar ages using CALIB 7.1 software (Reimer et al., 2013) with a reservoir age calculated from the Marine Reservoir Correction Database (http://calib.qub.ac.uk/marine/). Four sites near the Okhotsk Sea were selected (Reimer et al., 2013). The calculated weighted mean ΔR value was 450 ± 90 years. Radiocarbon results are listed in Supplementary Table 1.

ITRAX data show that Ba and Ti are negatively correlated with each other through the whole study section (r^2 = 0.58, Fig. 2). Ba and Ti intensities vary from 340-680 counts and 1100-4800 counts, respectively. ITRAX data have also been confirmed by traditional XRF measurements with lower time resolution (Liu et al., 2006). The log (Ba/Ti) ratio was correlated with LR04 for the upper 7-m and shows a good correlation with other physical parameters, including magnetic susceptibility (Chou et al., 2011), color reflectance (Bassinot and Chen, 2002) and coarse fraction (C.F., this study; Fig. 2). We assumed the log (Ba/Ti) ratio to represent a biological/terrestrial input ratio for our study site and this ratio varies with glacial/interglacial (G/IG) sea level changes due to global ice volume variations. During glacial periods, the west and north parts of the continental shelf were exposed in the Okhotsk Sea and more terrestrial sediment was transported to the central basin. On the other hand, during intervals of sea level rise, the central Okhotsk Sea became a region associate with a major biogenic bloom. Such biogenic/terrestrial distributions are supported by a previous surface sediment study (Strakhov et al., 1961). The similarity of the log(Ba/Ti) ratio of Site MD01-2414 to the LR04 is shown in Fig. 3H, and it persists for older intervals (Supplementary Fig. 1). The LR04 time is based on comparison to the Imbrie and Imbrie (1980) ice model, and the fit for the last glacial cycle is excellent between the model, LR04, and the log(Ba/Ti) ratio. The Imbrie and Imbrie (1980) model is delayed relative to insolation, and the Okhotsk Sea can be assumed to have reacted to insolation no more than large Northern

Hemisphere ice sheets. A shift by half a precession cycle (or more) is, therefore, not considered realistic. Thus, we correlate log(Ba/Ti) directly to LR04, with no lags, and the magnetic susceptibility and major paleo-polar reversal events support this age model for the whole sediment section back to 1.55 million years ago (Supplementary Fig. 1).

The average sedimentation rate in core MD01-2414 is 9.5 cm kyr^{-1} in the upper 235 cm, which indicates some piston stretching during the coring process. For the rest of the sections, sedimentation rates are 2–4 cm kyr^{-1}, similar to that found for nearby sites (Gorbarenko et al., 2010; Nürnberg et al., 2011).

3.4 Sea ice and phytoplankton biomarkers

Biomarker analysis was concentrated on the sea ice proxy IP_{25} (Belt et al., 2007; Belt and Müller, 2013) and a further highly branched isoprenoid (HBI) lipid associated with certain pelagic diatoms (HBI III; Belt et al., 2015). In the absence of a detailed surface sediment-based calibration, we refrained from using PIP_{25} data and, instead, focus on the distributions of the individual biomarkers. Part of the interpretation described here is based around the absence of IP_{25} in certain sediment horizons. In some previous investigations, absent IP_{25} has been interpreted in terms of representing either ice-free or permanent ice cover, although this is likely an over-simplification, not least as IP_{25} has been reported in regions of near permanent ice cover in the central Arctic Ocean (Xiao et al., 2015). To distinguish between these two extreme conditions of sea ice cover, here we use a combination of absent IP_{25} alongside HBI III and biogenic opal data (Liu et al., 2006), the latter parameter having been used previously in the neighboring western Bering Sea to identify intervals of higher productivity associated with open water settings (Méheust et al., 2016). More recently, the combined IP_{25}, HBI III and biogenic opal approach was used to reveal changes in sea ice dynamics across the Mid-Pleistocene Transition, also from the Bering Sea (Detlef et al., 2018). Further indications of ice-free settings have been inferred from accompanying SST data, also described herein.

IP_{25} and HBI III concentration data were obtained using methods described previously (e.g. Belt et al., 2015). Briefly, 2–3 g of freeze dried sediment material was extracted (dichloromethane/methanol; 3 x 12 mL; 2:1 v/v) by ultrasonication (15-min) and centrifugation (2500 rpm; 1 min) following addition of internal standards (9-octylheptadec-8-ene, 9-OHD, 10 µL; 10 µg mL^{-1}) for quantification purposes. Dried (nitrogen) total organic extracts were re-dissolved in hexane (ca. 1 mL) and purified using column chromatography (silica), with IP_{25} and HBI III (hexane; 6 mL) collected as a single fraction. Non-polar lipid fractions were further separated into saturated and unsaturated hydrocarbons using glass pipettes containing silver ion solid phase extraction material (Supelco Discovery® Ag-Ion). Saturated hydrocarbons were eluted with hexane (1 mL), while unsaturated hydrocarbons (including IP_{25} and HBI III) were eluted with acetone (2 mL). All fractions were analyzed using gas chromatography–mass spectrometry (GC–MS) and operating conditions were as described previously (Belt et al., 2015). Mass spectrometric analyses were carried out either in total ion current or single ion monitoring mode. Identification of individual lipids was achieved by comparison of their characteristic GC retention times and mass spectra with those of reference compounds. Lipid quantification was achieved by dividing peak area integrations of selected ions (*m/z* 350 (IP_{25}); 346 (HBI III)) by those of the internal standard (*m/z* 350 (9-OHD)) in single ion monitoring mode, with these ratios then normalized according to their respective instrumental response factors and sediment masses (Belt et al., 2015). Analytical reproducibility was monitored by co-analyzing homogenized sediment material with known biomarker abundance (every 14–16 sediment samples extracted, analytical error 7%, n = 6). In surface sediment samples from the Okhotsk Sea, the occurrence of IP_{25} and HBI III reliably reflect modern seasonal sea ice extent (Fig. 1, and Supplementary Fig. 2). Similar concentrations of HBI III in Holocene and MIS 5e indicate that the preservation is good throughout the study period (Fig. 3C).

3.5 TEX^{L}_{86} summer sea surface temperature proxy.

Sediment material (1–10 g) was freeze-dried and homogenized by mortar and pestle. The sediments were extracted by Dionex accelerated solvent extraction (DIONEX ASE 200) using a mixture of dichloromethane (DCM)/methanol (MeOH) (9:1, v/v) at a temperature of 100°C and a pressure of 7.6 x 10^6 Pa. The extracts were separated by Al_2O_3 column chromatography using hexane/DCM (9:1, v/v), hexane/DCM (1:1, v/v) and DCM/MeOH (1:1, v/v) as subsequent eluents. The polar fraction (DCM/MeOH) was dried under N_2, dissolved in hexane/isopropanol (99:1, v/v), and filtered using a 0.4 µm Polytetrafluoroethylene filter prior to injection as described by Hopmans et al. (2016).

Glycerol dialkyl glycerol tetraethers (GDGTs) were analyzed using an Agilent 1260 ultra high performance liquid chromatography (UHPLC) coupled to a 6130 quadrupole mass selective detector in selected ion monitoring mode. Separation was achieved on two UHPLC silica columns (unbonded ethylene bridged hybrid hydrophilic interaction chromatography columns, 2.1 x 150 mm, 1.7 µm; waters) in series, fitted with a 2.1 x 5 mm pre-column of the same material (waters) and maintained at 30°C. GDGTs were eluted isocratically using a two solvent gradient system (solvent A=hexane; solvent B= hexane:isopropanol (9:1, v/v)). Initial conditions employed 18% solvent B for 25-min followed by a linear gradient to 35% B over the next 25-min, then a linear gradient to 100% B over 30-min. Flow rate was 0.2 ml min^{-1}, resulting in a maximum back pressure of 230 bar for this chromatographic system. Total run time was 90-min with a 20-min re-equilibration. Source settings were identical to Schouten et al. (2007). Detection was achieved using atmospheric pressure positive ion chemical ionization mass spectrometry analysis of the eluent. Conditions were: nebulizer pressure 60 psi, vaporizer temperature 400°C, drying gas (N_2), flow 6 L min^{-1}, temperature 200°C, capillary voltage -3 kV, corona 5 µA (~3.2 kV). GDGTs were detected via single ion monitoring of their [M + H]+ ions (*m/z* = 1022, 1036, 1050, 1292, 1296, 1298, 1300, 1302) and quantified by integration of the peak areas.

The TEX^L_{86} proxy was proposed as a proxy to estimate SSST in the central Okhotsk Sea (Kim et al., 2010) and equations are listed as below:

$$TEX^L_{86} = \log([GDGT\text{-}2])/([GDGT\text{-}1]+[GDGT\text{-}2]+[GDGT\text{-}3])$$

$$SSST\text{-}TEX^L_{86} = 46.9 + 67.5 \times TEX^L_{86}$$

3.6 Time series analyses

Cross spectral analysis was done using AnalySeries (Paillard et al., 1996) and its implemented Blackman-Tukey method using a Bartlett window. Cyclic variations in the IP_{25} and SSST data were identified (Supplementary Table 2; Fig. 5; Taner, 1992; Meyers, 2014). IP_{25} lags precession by ca. 6-kyr (and lead Northern Hemisphere (NH) summer (June-July-August) insolation by a similar amount, Supplementary Table 2). Precession filters represent Taner filters using cut-off frequencies of 0.041 and 0.054

and a roll-off rate of 10^{54} (Fig. 5; Taner, 1992; Meyers, 2014). Note that the limited length of the time series limits precise phase statements.

3.7 Model simulations

To study the time-evolving aspects of orbital and greenhouse gas-driven climate change during glacial cycles, we conducted transient numerical modelling experiments using the earth system model LOVECLIM (Goose et al., 2010). LOVECLIM is a coupled ocean-atmosphere-sea ice-vegetation model. The ocean-sea ice component of LOVECLIM consists of a free-surface Ocean General Circulation Model with a 3° x 3° horizontal resolution coupled to a dynamic-thermodynamic sea-ice model (Fichefet and Morales Maqueda, 1997). The ocean and the sea-ice model use identical horizontal grids. The sea-ice model allows for the presence of open water areas (leads and polynyas) within an ice-covered ocean grid box. The fraction of a grid box covered by ice (sea-ice index) is computed from the heat budget of the open water area in this grid cell (Fichefet and Morales Maqueda, 1997). The sea-ice index is typically given as a number between zero and one with zero referring to ice-free conditions and one to a fully ice-covered grid cell.

The transient simulations were forced by time-dependent boundary conditions for orbital parameters, atmospheric greenhouse gas concentrations, NH ice sheet-orography and albedo following the methodology described in Timmermann et al. (2014). The time- and latitude-dependent orbital forcing was calculated according to Berger (1978). Atmospheric greenhouse gas concentrations (GHG) are prescribed according to reconstructions from EPICA Dome C for CO_2 (Lüthi et al., 2008) as well as CH_4 and N_2O (EPICA community members, 2004). Orbital forcing and atmospheric GHG concentrations are updated every model year. The ice sheets in the NH are prescribed according to Ganopolski and Calov (2011). The forcing is applied with an acceleration factor of 5 which compresses 784,000 years into 156,000 model years. This acceleration factor is appropriate for quickly equilibrating surface variables. The model simulation presented here is an updated version of the one presented in Timmermann et al. (2014) and uses a higher climate sensitivity (~4 K per CO_2-doubling). As a result, glacial-interglacial surface temperature amplitudes are simulated more realistically (Timmermann and Friedrich, 2016).

In addition to the full-forcing simulation described above, four sensitivity simulations were designed to elucidate the individual contributions by GHGs, NH ice sheets and orbital parameters to glacial-interglacial climate change. The first sensitivity simulation used transient forcing as described above but constant preindustrial atmospheric GHG concentrations. The "GHG effect" was then calculated as the difference between the simulation using the full forcing and this simulation. The second sensitivity simulation used transient forcing as described above but constant preindustrial NH ice sheets (extent and albedo). The "NH ice sheet effect" was calculated as the difference between the full-forcing simulation and this simulation.

The two remaining simulations were designed to study the role of orbital forcing under warm and cold climate respectively. For both simulations, transient orbital parameters are used. However, one simulation was run under constant pre-industrial atmospheric CO_2 concentration of 280 ppm whereas the second simulation uses a constant atmospheric CO_2 concentration of 200 ppm. It should be noted, however, that the forcing contributions cannot be deconvoluted entirely. Since variations in atmospheric GHG concentrations and NH ice sheets are actually feedbacks of the earth system, their temporal evolutions are ultimately driven by changes in orbital forcing.

4. Results and Discussion

4.1 Subarctic Pacific summer sea surface temperature and sea ice variations

Organic geochemical proxy analysis shows dramatic G/IG cycles in both sea ice extent and SSST (Fig. 3A, E). The absence of IP_{25} during MIS 5e (130-118 ka, Fig. 3B) and the majority of the Holocene (10-3 ka, Fig. 4), coupled with highest TEX^L_{86}-derived SSST (10.7–13.6 °C, Fig. 3E) and open water productivity indicators (HBI III and biogenic opal; Fig. 3C, D), provide clear indication of ice-free conditions during these two interglacials. TEX^L_{86}-based SSST values for the late Holocene section of MD01-2414 (12.8–13.7 °C) are similar to that of the modern temperature of 13°C (Fig. 4) (Luchin et al., 2009; Seki et al., 2014), while the absence of IP_{25} reflects that the study site was located beyond the position of recent average sea ice extent (Fig. 1; Supplementary Fig. 2). The modelled November sea ice index is also lowest during late MIS 5e and during the Holocene, while SSST data extracted from the simulations also reflect the trend of the TEX^L_{86}-derived SSST during the past 130 ka, albeit with a slight shift in absolute values (Supplementary Fig. 3). In contrast, the variable occurrence of

IP_{25} and substantially lower SSST (3–4 °C) and concentrations of open water productivity indicators during 117-30 ka indicates that seasonal (at least) sea ice cover prevailed during most of the MIS 5d-5a and last glacial periods (Fig. 3A, E), supported further by the observation of maxima in the modelled November sea ice index (Fig. 3B).

4.2 Precession-cycle control of Okhotsk sea ice change

When examined in more detail, the proxy and model-based sea ice extent in the central Okhotsk Sea during 117-30 ka shows a cycle of sea ice expansion and retreat that follows generally the same trend as local autumn insolation (53°N September–November, SON). In contrast, no satisfactory trend was identified between proxy/model data and other seasonal insolation (i.e. spring/summer/autumn). The general occurrence of IP_{25} throughout this interval is, however, punctuated by four intervals where IP_{25} is absent. For three of these (i.e. MIS 5c (~97 ka), 5a (~75 ka) and early MIS 3 (~55 ka)), HBI III is also relatively low (but quantifiable) and coincides with low–intermediate values of biogenic opal and SSST (Fig. 3). We interpret these findings as indicative of extremely low or absent sea ice at these times, with generally lower SST and productivity, at least in comparison with the relatively warm and productive MIS 5e and Holocene. In support of this conclusion, relatively low (November) sea ice extent is also observed in the modelled data (Figs. 3B, 4B). Although the boundary conditions associated with IP_{25} presence are not currently fully understood, the production of this biomarker by certain sympagic diatoms during the spring bloom (Brown et al., 2011) likely requires that sea ice cover extends at least beyond the winter months in order for this biomarker to provide a positive signature in underlying sediments. Further, IP_{25} concentration in surface sediments from other regions is generally positively related to the extent of the overlying spring sea ice cover, even though a lower limit threshold has not, as yet, been identified. Indeed, the majority of the previously reported IP_{25} data show lowest concentrations (bordering on limits of quantification in some cases) for subarctic locations characterized by low (e.g. <20%) spring sea ice extent, including the Okhotsk Sea (Supplementary Fig. 2), the neighboring Bering Sea (Méheust et al., 2013) and the Barents Sea in the eastern subarctic (Köseoğlu et al., 2017). As such, it is feasible that some regions experiencing extremely low spring sea ice concentration (e.g. <10%), or sea ice of relatively short seasonality, may not be amenable for study using the IP_{25} method. Further, not all sea ice diatoms produce IP_{25}, even if the known producers are considered widespread (Brown et al., 2014). This potentially explains, in part, the absence of IP_{25} in the Holocene record of MD01-2414 despite previous reports of some sea ice diatoms during this interval from the same core (Wang and Wang, 2008).

An alternative interpretation of the biomarker data for the three intervals MIS 5c, 5a and early MIS 3 is that permanent sea ice cover prevailed at these times. However, we consider this suggestion unlikely for the following reasons. First, we consider this end-member interpretation for absent IP_{25} to be less robust than that of ice-free conditions, especially since IP_{25} has been identified in some regions of the central Arctic Ocean experiencing near permanent sea ice cover (Xiao et al., 2015). As such, there are a number of reasons why the interpretation of IP_{25} absence for sea ice reconstruction purposes is more challenging than that of its presence. Second, improvements to understanding the IP_{25} absence scenario can generally be made through parallel measurement of proxies characteristic of open water conditions, including some phytoplankton biomarkers (e.g. Müller et al., 2009, Belt and Müller, 2013; Belt et al., 2015; Hoff et al., 2016; Méheust et al., 2016). Here, non-zero concentrations of phytoplankton-derived HBI III (and moderate biogenic opal content) are observed during MIS 5c (~97 ka), 5a (~75 ka) and early MIS 3 (~55 ka) (Supplementary Fig. 4), which is difficult to rationalize in terms of permanent ice conditions. In fact, despite their relatively low values, the individual HBI III concentrations during these intervals are all higher than the mean value for the interval 117-30 ka (ca. 0.05 ng g^{-1}), which is characterized mainly by variable seasonal sea ice cover (Supplementary Fig. 4). Such an observation is, therefore, more consistent with intervals of low/absent sea ice during MIS 5c, 5a and 3, and with generally lower SSST and productivity compared to MIS 5e and the Holocene (vide supra), each of which are bracketed by longer intervals of more extensive sea ice extent. Third, we note that although HBI III was present in all surface sediments from across the Okhotsk Sea (Supplementary Fig. 2), its concentration was highly dependent on location (Supplementary Table 3). However, the HBI III concentrations in two surface sediments from sites in the central Okhotsk Sea (i.e. near MD01-2414) that experience low sea ice cover in modern times, and where IP_{25} was also absent (i.e. stations 55-19-2 and 55-24-2; Supplementary Fig. 2 and Supplementary Table 3), are similar (ca. 0.2-0.3 ng g^{-1}) to those found for intervals MIS 5c (~97 ka), 5a (~75 ka) and early MIS 3 (~55 ka) in MD01-2414. These core-top data thus provide some potential context to those found for during MIS 5c, 5a and 3 in MD01-2414.

On the other hand, absent IP_{25} and low HBI III during certain intervals in MIS 2–4 may, instead, reflect increased biomarker degradation downcore. While this may be a contributing factor, the general occurrence of both IP_{25} and HBI throughout MIS 2–4 and the subsequent large increase in HBI III concentration during MIS 5e to values similar to those seen in the late Holocene, suggests that any climatic influence likely exceeds that resulting from diagenesis (Stein et al., 2016). Higher concentrations of IP_{25} and HBI III in older sedimentary sequences (relative to those found in younger sections of the same cores) have also been reported in previous studies (e.g. Belt et al., 2015), where climatic influences were considered to be the controlling factors of biomarker distributions. As such, we conclude that the three intervals of absent IP_{25} during MIS 5c (~97 ka), 5a (~75 ka) and early MIS 3 (~55 ka) represent periods of low/absent sea ice (as also seen in the modelled data), but otherwise relatively cool sea surface conditions and low productivity. These intervals coincide with precession minima and maximum insolation during autumn (Fig. 3B), which contrasts intervals of IP_{25} occurrence when insolation was lower.

In contrast, we suggest that the absence of sea ice (IP_{25}) and open water (HBI III) biomarkers at ~30 ka is more consistent with the presence of perennial (or near-perennial) sea ice cover at this time, based on related findings and interpretations in previous studies from other regions (e.g. Müller et al., 2009; Hoff et al., 2016). Although our observation is based on only one data point, and the related SSST and biogenic opal data were not obtained from exactly the same sediment horizons (albeit both were relatively low), our interpretation is consistent with earlier records of lithological, magnetic, and floral assemblages from the Okhotsk Sea (Sakamoto et al., 2005; Khim et al., 2012; Nürnberg et al., 2011) at ~30 ka and from the neighboring Bering Sea (Max et al., 2014) based on IP_{25} and other geochemical data. Spatial and time differences within the Okhotsk Sea could be attributable to the different sources of IRD sediment source dynamics (Nürnberg et al., 2011) and further combined organic proxy, sedimentological, and inorganic geochemical analyses need to be conducted in different areas to evaluate the source dynamics during the past G/IG cycles in the Okhotsk Sea.

The variability in IP_{25} from 120 to 30 ka, therefore, likely reflects reversible transitions between very low (IP_{25} absent), seasonal (IP_{25} present and variable), and possibly near-perennial (IP_{25} absent) sea ice cover, with a cyclicity trend identified in the 20-kyr precession forcing (Fig. 5; Supplementary Table 2). These transitions are supported by previous and related observations in the northern Fram Strait during the last 22 ka (Müller et al., 2009) and Heinrich events in the Nordic Seas over the last 90 ka (Holf et al., 2016).

Overall, the apparent local autumn insolation control on the sea ice extent in the Okhotsk Sea suggests sensitivity to external (insolation) forcing. Further, since current sea ice formation in the Okhotsk Sea generally occurs somewhat later than autumn (typically in December), a further outcome of these findings is that any positive identification of seasonal sea ice in the proxy (i.e. IP_{25}) and modeled data likely implies intervals of earlier freeze-up, at least compared to modern times. Consistent with this, although IP_{25} is produced by certain diatoms during the spring, its sedimentary occurrence normally reflects regions of autumn sea ice presence (see Belt and Müller, 2013 for a review). Precession filters also align well between IP_{25} data and the model-derived November sea ice index (Fig. 5). However, the limited length and resolution of the time series make quantification of (cross-)spectral analyses challenging, and results rely mainly on the clear cyclic expression of proxy data as observed, filtered, and compared to autumn insolation (Figs. 5, 6, 8).

Freshwater input from the Amur River has also been proposed as a potential controlling factor of sea ice formation in the Okhotsk Sea in modern and last G/IG cycles (Sakamoto et al., 2005; Harada et al., 2008). Further, it has been suggested that there may have been a strong coupling between the East Asian summer monsoon (EASM) and the amount of freshwater input on millennial-orbital timescales. However, there is no clear relationship between the composite speleothem $\delta^{18}O$ record reported by Cheng et al. (2016) and our IP_{25} record from the central Okhotsk Sea during the past 130 ka (Fig. 3A, G), even though both records exhibit a strong precession cycle. There is also no clear link between periods of sea ice expansion (high IP_{25}) in the central Okhotsk Sea (this study) and intervals of northward shifting of East Asian monsoons/Intertropical Convergence Zone (ITCZ) precipitation during the past 130 ka (Cheng et al., 2016).

During the last termination, however, there is a near synchronous (within the error of current age model) increase in IP_{25} with a period of stronger EASM during the B/A period (~15 ka). SSST and biogenic opal increased slightly earlier and HBI III concentration increased coeval with IP_{25}. These proxy data suggest rapid fluctuations between open water and seasonal sea ice covered conditions, with high surface productivity during the B/A period, similar to previous studies in the subarctic Pacific Ocean (Max et al., 2012). The relationship between EASM and sea ice variations on millennial-orbital timescales, however, still needs further observational and physical simulation studies.

4.3 CO_2 control for precessionally-paced sea ice

The observation that sea ice free conditions existed throughout MIS 5e, even when autumn insolation reached a minimum, together with near-perennial sea ice cover despite only relatively low insolation ~30 ka, suggests that forcing(s) other than insolation controlled sea ice dynamics during these intervals. Coincidence of ice-free conditions with atmospheric CO_2 levels in excess of 260 ppm (Figs. 3F, 4F) during both MIS 5e and the Holocene suggests that such concentrations potentially represent an important threshold that influences sea ice retreat in the central Okhotsk Sea. Similarly, maximum sea ice extent in both proxy and simulated records are only attained during periods of lowest CO_2 (180–200 ppm) in combination with relatively low insolation (~30 ka, Figs. 3, 5, 6). In contrast, in the low-to-medium CO_2 range (190–260 ppm), which is present in MIS 3, 5a and 5c, ice-free conditions are paced by precession and controlled by maximum autumn insolation (Fig. 6). Our proxy-model results in the central Okhotsk Sea therefore suggest that the major controlling factors of seasonal sea ice extent are from both external orbital-driven insolation and internal CO_2 concentration forcings on orbital timescales (Fig. 8). On the other hand, the absence of any clear relationship between sea ice and atmospheric CH_4 (not shown) suggests that methane was not a significant factor during these interglacials, at least. This is potentially due to the fact that the total radiative energy variations from atmospheric CH_4 is believed to be less than 5% of the total radiative energy of greenhouse gases in recent G/IG cycles (Lo et al., 2017).

4.4 Orbital pacing and CO_2 threshold mechanisms revealed by transient model simulations

The model sensitivity runs deciphering the contributions of different climatic forcings (orbital, CO_2, and NH ice sheet) show that sea ice variations can be regarded mainly as a superposition of the CO_2 effect and orbital forcing, with a small contribution from Northern Hemispheric ice sheets (Fig. 6B). During the sea ice-free MIS 5e, (130–117 ka), autumn insolation varied by nearly 70 W m^{-2}, yet the November sea ice index varied by less than 0.1 unit, suggesting that orbital forcing was muted during this period of high atmospheric CO_2 concentration (Figs. 6B, 8).

For the sensitivity simulation for orbital forcing under a warm climate (red squares in Fig. 7), a linear regression between insolation and the sea ice index yields a slope of -0.02/ W m^{-2}, pointing to a relatively weak impact of insolation changes under high atmospheric CO_2 conditions (CO_2 = 280 ppm), even during periods of large insolation changes, such as during MIS 5e (Figs. 6B, 8). However, the impact of orbitally-driven insolation changes on sea ice becomes larger for the lower atmospheric CO_2 condition run (CO_2 = 200 ppm, -0.03/ W m^{-2}, triangles in Fig. 7).

Under medium CO_2 concentrations during MIS 5a-5d and the last glacial period, insolation forcing and the CO_2 forcing are both important. Thus, precession-paced insolation maxima result in brief episodes of sea ice minima (Fig. 6B), although when the amplitude of the insolation forcing is weak, CO_2 variations appear to be the main driver of the simulated sea ice index during MIS 3 and 4. The maximum in simulated sea ice coverage coincides with minimum CO_2 values of ~190 ppm at ~30 ka. Local SON insolation increased towards the last glacial maximum, resulting in slightly decreased sea ice extent when compared to ~30 ka.

5. Conclusions

In this study, we reconstructed SSST and sea ice variations in the central Okhotsk Sea over the last 130 ka by combination of novel organic geochemical proxies including TEX^{L}_{86} and IP_{25}. To reveal the physical mechanisms responsible for the near-surface oceanographic changes, numerical simulation data and sensitivity runs were also performed. Our geochemical proxy analyses and transient simulation data show that the precession pacing by local autumn insolation was a major control over variation in sea ice extent during the past 130 ka. Greenhouse gas (mainly CO_2) induced atmospheric radiative forcing acts as a further threshold for sea ice absence when CO_2 concentration exceeded ~260 ppm and for extensive sea ice cover when CO_2 concentration fell below 190 ppm. The dominant driver of, respectively, sea ice free conditions during MIS 5e and perennial sea ice conditions ~30 ka is thus atmospheric radiative forcing. Therefore, we suggest a combined orbital and greenhouse gas control over sea ice variations in the central Okhotsk Sea during the past 130 ka.

Near-surface oceanographic conditions (i.e. sea ice and SSST) may also have been influenced by the extent of fresh water input from the Amur River. However, further regional studies including seasonal temperature and more reliable freshwater records before the role of this potential forcing can be fully understood.

Acknowledgements

This project was supported by grants of the Ministry of Science and Technology (MOST), Taiwan ROC (10-2119-M-002-003, 104-2917-I-564-046, 105-2119-M-002-001), State Key Laboratory of Isotope Geochemistry, Guangzhou Institute of Geochemistry, Chinese Academy of Sciences start-up fund (SKLaBIG-QD-16-04) and National Natural Science Foundation (41773116). MD01-2414 sediment samples were generously provided by Taiwan Ocean Research Institute (TORI). We thank the University of Plymouth for financial support. S.S. and J.L. were supported by European Research Council (ERC) under the European Union's Seventh Framework Program (FP7/2007-2013) ERC grant agreement [339206] and by the Netherlands Earth System Centre (NESSC) funded by the Dutch Ministry of OCW. Finally, we thank two anonymous reviewers and the Editor for providing extremely positive feedback on the original version of this manuscript, with further suggestions that improved its clarity in final form.

References

Bassinot, F., Chen, M.-T., 2002. Physical properties of sediment core MD01-2414. doi:10.1594/PANGAEA.80047.

Belt, S.T., Massé, G., Rowland, S.J., Poulin, M., Michel, C., LeBlanc, B., 2007. A novel chemical fossil of palaeo sea ice: IP_{25}. Org. Geochem. 38, 16-27.

Belt, S.T., Cabedo-Sanz, P., Smik, L., Navarro-Rodriguez, A., Berben, S.M.P., Knies, J., Husum, K., 2015. Identification of paleo Arctic winter sea ice limits and the marginal ice zone: optimised biomarker-based reconstructions of late Quaternary Arctic sea ice. Earth Planet. Sci. Lett. 431, 127–139.

Belt, S.T., Müller, J., 2013. The Arctic sea ice biomarker IP_{25}: a review of current understanding, recommendations for future research and applications in palaeo sea ice reconstructions. Quat. Sci. Rev. 79, 9-25.

Berger, A., 1978. Long-term variations of daily insolation and quaternary climate change. J. Atmos. Sci. 35, 2362-2367.

Brown, T.A., Belt, S.T., Tatarek, A., Mundy, C.J., 2014. Source identification of the Arctic sea ice proxy IP_{25}. Nat. Commun. 5, 4197.

Cheng, H., Edwards, R.L., Sinha, A., Spötl, C., Yi, L., Chen, S., Kelly, M., Kathayat, G., Wang, X., Li, X., Kong, X., Wang, Y., Ning, Y., Zhang, H., 2016. The Asian monsoon over the past 640,000 years and ice age terminations. Science 534, 640-646.

Chou, Y.-M., Lee, T.-Q., Song, S.-R., Chen, K.-J., 2011. Magnetostratigraphy of marine sediment core MD01-2414 from Okhotsk Sea and its paleoenvironmental implications. Mar. Geol. 284, 149-157.

Detlef, H., Belt, S.T., Sosdian, S.M., Smik, L., Lear, C.H., Hall, I.R., Cabedo-Sanz, P, Husum, K., Kender, S., 2018. Changes in sea ice dynamics in the eastern Bering Sea during the Mid-Pleistocene climate transition. Nat. Commun. (in press).

EPICA community members, 2004. Eight glacial cycles from an Antarctic ice core. Nature 429, 623-628.

Ganopolski, A., Calov, R., 2011. The role of orbital forcing, carbon dioxide and regolith in 100 kyr glacial cycles. Clim. Past 7, 1415-1425.

Goosse, H., Brovkin, V., Fichefet, T., Haarsma, R., Huybrechts, P., Jongma, J., Mouchet, A., Selten, F., Barriat, P.-Y., Campin, J.-M., Deleersnijder, E., Driesschaert, E., Goelzer, H., Janssens, I., Loutre, M.-F., Morales Maqueda, M.A., Opsteegh, T., Mathieu, P.-P., Munhoven, G., Pettersson, E.J., Renssen, H., Roche, D.M., Schaeffer, M., Tartinville, B., Timmermann, A., Weber, S.L., 2010. Description of the Earth system model of intermediate complexity LOVECLIM version 1.2. Geosci. Model Dev. 3, 603-633.

Gorbarenko, S.A., Harada, N., Malakhov, M.I., Vasilenko, Y.P., Bosin, A.A., Goldberg, E.L., 2010. Orbital and millennial-scale environmental and sedimentological changes in the Okhotsk Sea during the last 350 kyr. Global Planet. Change 72, 79-85.

Harada, N., Sato, M., Sakamoto, T., 2008. Freshwater impacts recorded in tetraunsaturated alkenones and alkenone sea surface temperatures from the Okhotsk Sea across millennial-scale cycles. Paleoceanography 23, PA3201, doi:10.1029/2006PA001410.

Hoff, U., Rasmussen, T.L., Stein, R., Ezat, M.M., Fahl, K., 2016. Sea ice and millennial-scale climate variability in the Nordic seas 90 kyr ago to present. Nat. Commun. 7, 12247, doi:10.1038/ncomms12247.

Hopmans, E.C., Schouten, S., Sinninghe Damsté, J.-S., 2016. The improved chromatography on GDGT-based paleoproxies. Org. Geochem. 93, 1-6.

Huang, J.-J, Löwemark, L., Chang, Q., Lin, T.-Y., Chen, H.-F., Song, S.-R., Wei, K.-Y., 2016. Choosing optimal exposure times for XRF core-scanning: Suggestions based on the analysis of geological reference materials. Geochem. Geophy. Geosy. 17, 1558-1566.

Imbrie, J., Imbrie, J.Z., 1980. Modeling the climatic response to orbital variations. Science 207, 943-953.

Kashiwase, H., Ohshima, K.I., Nihashi, S., 2014. Long-term variation in sea ice production and its relation to the intermediate water in the Sea of Okhotsk. Prog. Oceanogr. 126, 21-32.

Khim, B.-K., Sakamoto, T., Harada, N., 2012 Reconstruction of surface water conditions in the central region of the Okhotsk Sea during the last 180 kyrs. Deep Sea Res. II 61-64, 63-72.

Kim, J.-H., van der Meer, J., Schouten, S., Helmke, P., Willmott, V., Sangiorgi, F., Koç, N., Hopmans, E.C., Sinninghe-Damsté, J.S., 2010. New indices and calibrations derived from the distribution of crenarchaeal isoprenoid tetraether lipids: Implications for past sea surface temperature reconstructions. Geochim. Cosmochim. Ac. 74, 4639-4654.

Kimura, N., Wakatsuchi, M., 2004. Increase and decrease of sea ice area in the Sea of Okhotsk: Ice production in coastal polynyas and dynamic thickening in convergence zones. J. Geophys. Res. 109, C9, doi:10.1029/2003JC001901

Köseoğlu, D., Belt, S.T., Smik, L., Yao, H., Panieri, G., Knies, J., 2018. Complementary biomarker-based methods for characterising Arctic sea ice conditions: A case study comparison between multivariate analysis and the PIP_{25} index. Geochim. Cosmochim. Ac. 222, 406–420. doi.org/10.1016./j.gca.2017.11.001.

Laskar, J., Robutel, P., Joutel, F., Gastineau, M., Correia, A.C.M., Levard, B., 2004. A long-term numerical solution for the insolation quantities of the Earth. Astron. Astrophys. 428, 261-285.

Lisiecki, L.E., Raymo, M.E., 2005. A Pliocene-Pleistocene stack of 57 globally distributed benthic $\delta^{18}O$ records. Paleoceanography 20, PA1003.

Liu, Y.-J., Song, S.-R., Lee, T.-Q., Lee, M.-Y., Chen, Y.-L., Chen, H.-F., 2006. Mineralogical and geochemical changes in the sediments of the Okhotsk Sea during deglacial periods in the past 500 kyrs. Global Planet. Change 53, 47-57.

Lo, L., Chang, S.-P., Wei, K.-Y., Lee, S.-Y., Ou, T.-H., Chen, Y.-C., Chuang, C.-K., Mii, H.-S., Burr, G.S., Chen, M.-T., Tung, Y.-H., Tsai, M.-C., Hodell, D.A., Shen, C.-C., 2017. Nonlinear climatic sensitivity to greenhouse gases over the past 4 glacial/interglacial cycles. Sci. Rep. 7, 4626, doi: 10.1038/s41598-017-04031-x.

Luchin, V., Kruts, A., Sokolov, V., Rostov, V., Rudykh, N., Perunova, T., Zolotukhin, E., Pischalnik, V., Romeiko, L., Hramushin, V., Shustin, V., Udens, Y., Baranova, O., Smolyar, I., Tarosh, E., 2009. Climatic Atlas of the North Pacific Seas: Bering Sea, Sea of Okhotsk, and Sea of Japan, NOAA Atlas NESDIS 67, U.S. Gov. Printing Office, Wash., D.C, p. 380 (CD Disc).

Lüthi, D., Floch, M.L., Bereiter, B., Blunier, T., Barnola, J.-M., Siegenthaler, U., Raynaud, D., Jouzel, J., Fischer, H., Kawamura, K., Stocker, T.F., 2008. High-resolution carbon dioxide concentration record 650,000-800,000 years before present. Nature 453, 379-382.

Max, L., Riethdorf, J.-R., Tiedemann, R., Smirnova, M., Lembke-Jene, L., Fahl, K., Nürnberg, D., Matul, A., Mollenhauer, G., 2012. Sea surface temperature variability and sea-ice extent in the subarctic northwest Pacific during the past 15,000 years. Paleoceanography 27, PA3213, doi:10.1029/2012PA002292.

Max, L., Tiedemann, R., Fahl, K., Nürnberg, D., Riethdorf, J.-R., 2014. Rapid shifts in subarctic Pacific climate between 138 and 70 ka. Geology 42, 899-902.

Méheust, M., Fahl, K., Stein, R., 2013. Variability in modern sea surface temperature, sea ice and terrigenous input in the sub-polar North Pacific and Bering Sea: Reconstruction from biomarker data. Org. Geochem. 57, 54-64.

Méheust, M., Stein, R., Fahl, K., Max, L., Riethdorf, J.-R., 2016. High-resolution IP_{25}-based reconstruction of sea-ice variability in the western North Pacific and Bering

Sea during the past 18,000 years. Geo-Marine Lett. 36, 101-111.

Mesquita, M.D., Hodges, K.I., Atkinson, D.E., Bader, J., 2011. Sea-ice anomalies in the Sea of Okhotsk and the relationship with storm tracks in the Northern Hemisphere during winter. Tellus A 63, 312-323.

Meyers, S.R., 2014. Astrochron: An R Package for Astrochronology Version 0.6.5.

Müller, J., Massé, G., Stein, R., Belt, S.T., 2009. Variability of sea-ice conditions in the Fram Strait over the past 30,000 years. Nat. Geosci. 2, 772-776.

Nishioka, J., Yasuda, I., Liu, H., Nakatsuka, T., Volkov, Y.N., 2014. Biogeochemical and physical processes in the Sea of Okhotsk and the linkage to the Pacific Ocean. Prog. Oceanogr. 126, 1-7.

Nürnberg, D., Dethleff, D., Tiedemann, R., Kaiser, A., Gorbarenko, S.A., 2011. Okhotsk Sea ice coverage and Kamchatka glaciation over the last 350 ka- Evidence from ice-rafted debris and planktonic $\delta^{18}O$. Palaeogr. Palaeoclimatol. Palaeoecol. 310, 191-205.

Ono, A., Takahashi, K., Katsuki, K., Okazaki, Y., Sakamoto, T., 2005. The Dansgaard-Oeschger cycles discovered in the upstream source region of the North Pacific Intermediate Water formation. Geophys. Res. Lett. 32, L11607, doi:10.1029/2004GL022260.

Paillard, D., Labeyrie, L., Yiou, P., 1996. Macintosh program performs time-series analysis, EOS Trans. 77, 379.

Reimer, P. J., Bard, E., Bayliss, A., Beck, J. W., Blackwell, P. G., Bronk Ramsey, C., Buck, C. E., Cheng, H., Edwards, R. L., Friedrich, M., Grootes, P. M., Guilderson, T. P., Haflidason, H., Hajdas, I., Hatté, C., Heaton, T. J., Hoffmann, D. L., Hogg, A. G., Hughen, K. A., Kaiser, K. F., Kromer, B., Manning, S. W., Niu, M., Reimer, R. W., Richards, D. A., Scott, E. M., Southon, J. R., Staff, R. A., Turney, C. S. M., and van der Plicht, J., 2013. IntCal13 and Marine13 radiocarbon age calibration curves 0–50,000 years cal BP. Radiocarbon, 55,1869–1887, https://doi.org/10.2458/azu_js_rc.55.16947, 2013.

Sakamoto, T., Ikehara, M., Aoki, K., Iijima, K., Kimura, N., Nakatsuka, T., Wakatsuchi, W., 2005. Ice-rated debris (IRD)-based sea-ice expansion events during the past 100 kyrs in the Okhotsk Sea. Deep-Sea Res. II 52, 2275-2301.

Schlitzer, R., 2017. Ocean Data View, odv.awi.de.

Schouten, S., Huguet, C., Hopmans, E.C., Kienhuis, M., Sinninghe Damsté, J.-S., 2007. Analytical Methodology for TEX_{86} paleothermometry by high-performance liquid chromatography/atmospheric pressure chemical ionization-mass spectrometry. Anal. Chem. 79, 2940-2944.

Seki, O., Bendle, J.A., Harada, N., Kobayashi, M., Sawada, K., Moossen, H., Inglis, G.N., Nagao, S., Sakamoto, T., 2014. Assessment and calibration of TEX_{86} paleothermometry in the Sea of Okhotsk and sub-polar North Pacific region: Implications for paleoceanography. Prog. Oceanogr. 126, 254-266.

Serreze, M.C., Stroeve, J., Barrett, A.P., Boisvert, L.N., 2016. Summer atmospheric circulation anomalies over the Arctic Ocean and their influence on September sea ice extent. A cautionary tale. J. Geophys. Res. Atmos. 121, 1463-11485.

Stein, R., Fahl, K., Schreck, M., Knorr, G., Forwick, M., Gebhardt, C., Jensen, L., Kaminski, M., Kopf, A., Matthiessen, J., Jokat, W., Lohmann, G., 2016. Evidence for ice-free summers in the late Miocene central Arctic Ocean. Nat. Commun. 7, 11148, doi:10.1038/ncomms11148.

Strakhov, N.M., Bezrukov, P.L., Yablokov, V.S., 1961. Recent precipitates in Seas and Oceans. Press of the Academy of Sciences USSR, Moscow, 644 pp. (in Russian).

Taner, M.T., 1992. In: Attributes revisted (Technical Report, Rock Solid Images, Inc), http://www.rocksolidimages.com/attributes-revisited/#_Toc328470897.

Timmermann, A., Friedrich, T., Timm, O.E., Chikamoto, M.O., Abe-Ouchi, A., Ganopolski, A., 2014. Modeling obliquity and CO_2 effects on Southern Hemisphere climate during the past 408 ka. J. Clim. 27, 1863-1875.

Timmermann, A., Friedrich, T., 2016. Late Pleistocene climate drivers of early human migration. Nature 538, 92-95.

Turner, J., Scott Hosking, J., Marshall, G.J., Phillips, T., Bracegirdle, T.J., 2016. Antarctic sea ice increase consistent with intrinsic variability of the Amundsen Sea Low. Clim. Dyn. 46, 2391-2402.

Veres, D., Bazin, L., Landais, A., Toyé Mahamadou Kele, H., Lemieux-Dudon, B., Parrenin, F., Martinerie, P., Blayo, E., Blunier, T., Capron, E., Chappellaz, Rasmussen, S.O., Severi, M., Svensson, A., Vinther, B., Wolff, E.W., 2013. The Antarctic ice core chronology (AICC2012): an optimized multi-parameter and multi-site dating approach for the last 120 thousand years. Clim. Past 9, 1733-1748.

Wang, W.-L., Wang, L.-C., 2008. Reconstruction of oceanographic changes based on the diatom records of the central Okhotsk Sea over the last 500000 years. Terr. Atmos. Ocean. Sci. 19, 403-411.

Xiao, X., Fahl, K., Müller, J., Stein, R., 2015. Sea-ice distribution in the modern Arctic Ocean: Biomarker records from trans-Arctic Ocean surface sediments. Geochim. Cosmochim. Ac. 155, 16–29.

Figure Captions

Fig. 1. Site location. Core MD01-2414 (53°11.77’N, 149°34.80’E, water depth 1123 m) is located in the Okhotsk Sea. The blue arrows indicate surface water circulation (WKC: West Kamchatka Current, ESC: East Sakhalin Current, and SWC: Soya Warm Current) and the dashed black line denotes the average position of modern seasonal sea ice extent, during the months of November to June. This map was generated with Ocean Data View (GMT) version 5 (Schlitzer, 2017).

Fig. 2. Age model of Site MD01-2414 for the upper 7 m. (A) ITRAX scanned log(Ba/Ti) ratio, (B) Ba, (C) Ti, (D) magnetic susceptibility in log scale (Chou et al., 2011), (E) b* (Bassinot and Chen, 2002), (F) coarse fraction (C.F., this study) in weight percent (this study), and (G) global benthic composite oxygen isotope curve (black curve, Lisiecki and Raymo, 2005) and sedimentation rate (orange). Dark yellow line represents 3-point running average. Green crosses and triangles represent radiocarbon dates and age model tie points, respectively.

Fig. 3. Geochemical proxy results from Site MD01-2414 during the past 130 ka. (E) SSST derived from TEX^{L}_{86} in red and 53°N June-July-August (JJA) insolation in pink (Lasakar et al., 2004). (A) IP_{25} concentration in gray. (B) model-derived Okhotsk Sea November sea ice index, and 53°N September-October-November (SON) insolation in

orange (Lasakar et al., 2004) (C) HBI III (green) and concentration. (D) MD01-2414 opal content (dark yellow, Liu et al., 2006). (F) Atmospheric CO_2 (Lüthi et al., 2008) in AICC2012 timescale (Veres et al., 2013). (E) SSST derived from TEX^{L}_{86} in red and 53°N June-July-August (JJA) insolation in pink (Laskar et al., 2004). (G) Compiled Chinese speleothem $\delta^{18}O$ record (Cheng et al., 2016). (H) XRF scanned log(Ba/Ti) in purple and LR04 benthic oxygen isotope curve in black (Lisiecki and Raymo, 2005). Semi-quantitative sea ice conditions from: sea ice retreat (white), sea ice expand (gray), and possible perennial sea ice (blue with question mark). Slash bar in (E) represents critical CO_2 threshold from 260 to 280 ppm. Marine isotope stages (MIS) are listed in Fig. 3H.

Fig. 4. Geochemical proxy results from Site MD01-2414 during the past 29 ka. Captions and color bars are the same as Fig. 3. Black triangles represent AMS ^{14}C dates with 2σ error bars in Supplementary Table 1. YD, B/A, and H1 represent Younger Dryas, Bølling-Allerød (yellow bar), and Heinrich stadial 1 periods, respectively.

Fig. 5. Precession filters comparison between model and proxy data. Data (all black) of the modelled November Sea ice index (A), the IP_{25} (B) and precession (C), together with respective precession filters (all red, Taner filters using cut-off frequencies (1 kyr^{-1}) of 0.041 and 0.054 and a roll-off rate of 10^{54} (Taner, 1992; Meyers, 2014) plotted versus time.

Fig. 6. Individual contributions by variations in GHG, orbital parameters and NH ice sheets. (A) 53°N SON insolation (Laskar et al., 2004). (B) Transient model results for Okhotsk Sea November sea ice index anomaly with respect to 1-kyr for full-forcing (black solid), GHG-effect (red dashed), orbital effect (green dashed) and effect of NH ice sheet (purple dashed). Background shading and MIS numbers are the same as Fig. 3.

Fig. 7. Scatter plot of transient model results for Okhotsk Sea November sea-ice index versus 53°N SON insolation (W m^{-2}) (Laskar et al., 2004) for full-forcing (circles) and orbital effect for cold and warm climates (squares and triangles). Corresponding atmospheric CO_2 concentrations (ppm) are shaded. The orbital-effect simulations use

only transient orbital parameters and constant atmospheric CO_2 concentration of either 280 ppm (squares) or 200 ppm (triangles) respectively. Please see Section 3.7 (Model simulations) for details regarding the model simulations.

Fig. 8. Schematic figure of the of CO_2 level and insolation forcings on sea ice variability in the central Okhotsk Sea during the past 130 ka.

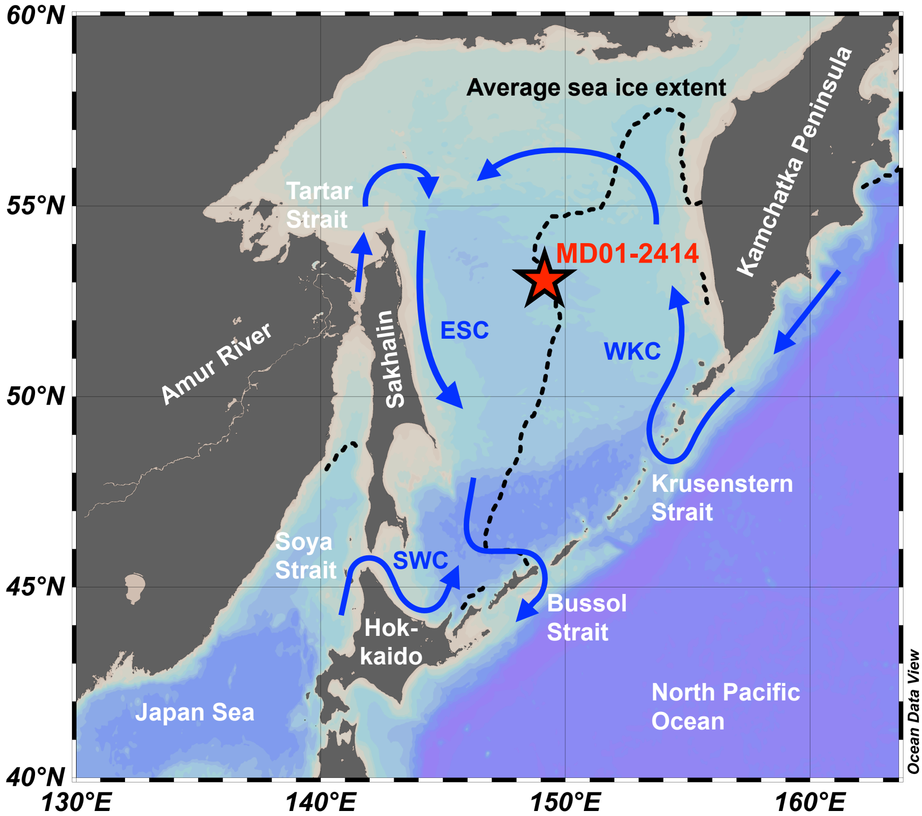
60°N
55°N
50°N
45°N
40°N
130°E
140°E
150°E
160°E
Average sea ice extent
Tartar Strait
MD01-2414
Kamchatka Peninsula
Amur River
Sakhalin
ESC
WKC
Krusenstern Strait
Soya Strait
SWC
Hok-kaido
Bussol Strait
Japan Sea
North Pacific Ocean
Ocean Data View

Figure 1

863

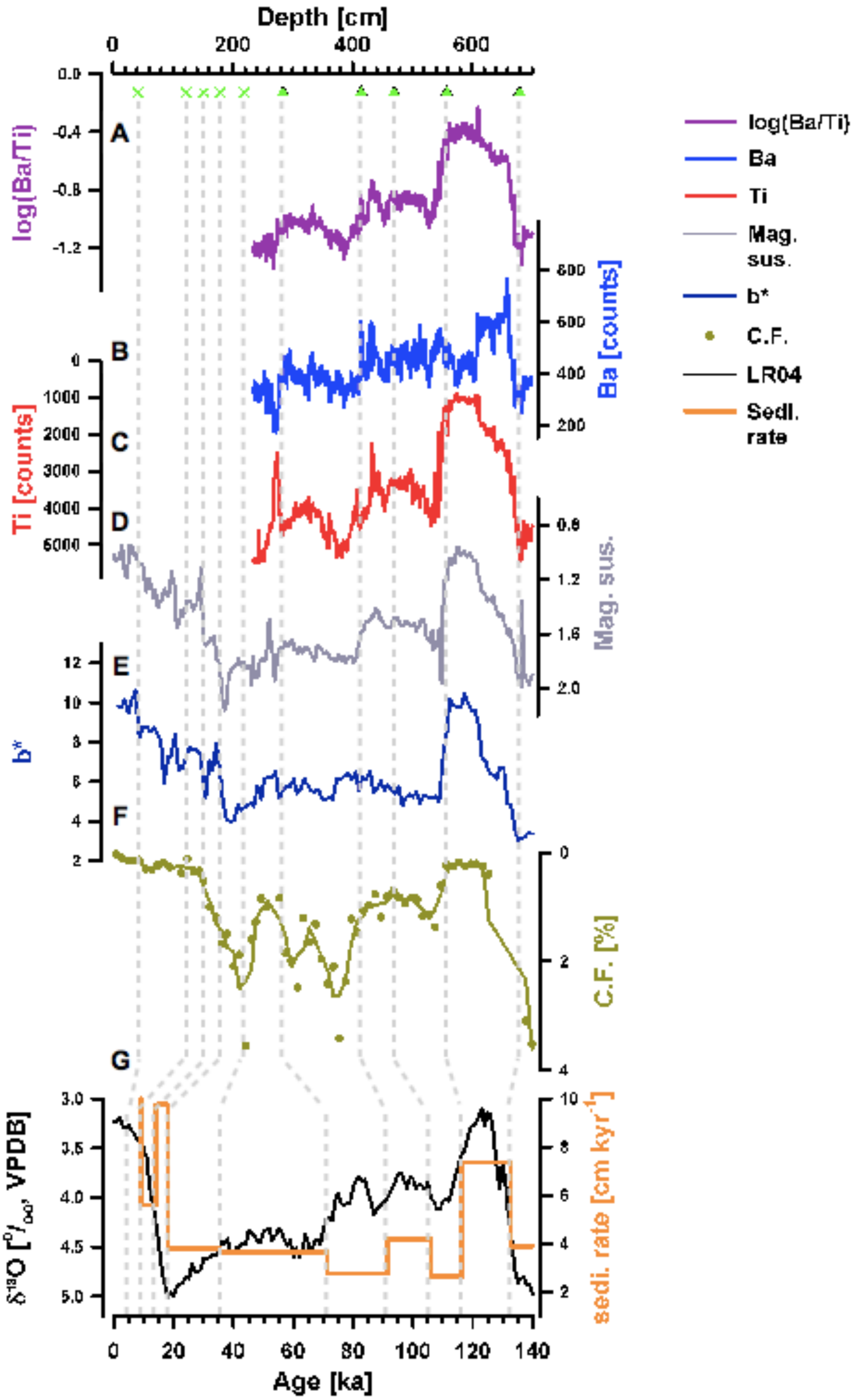

864

865 **Figure 2**

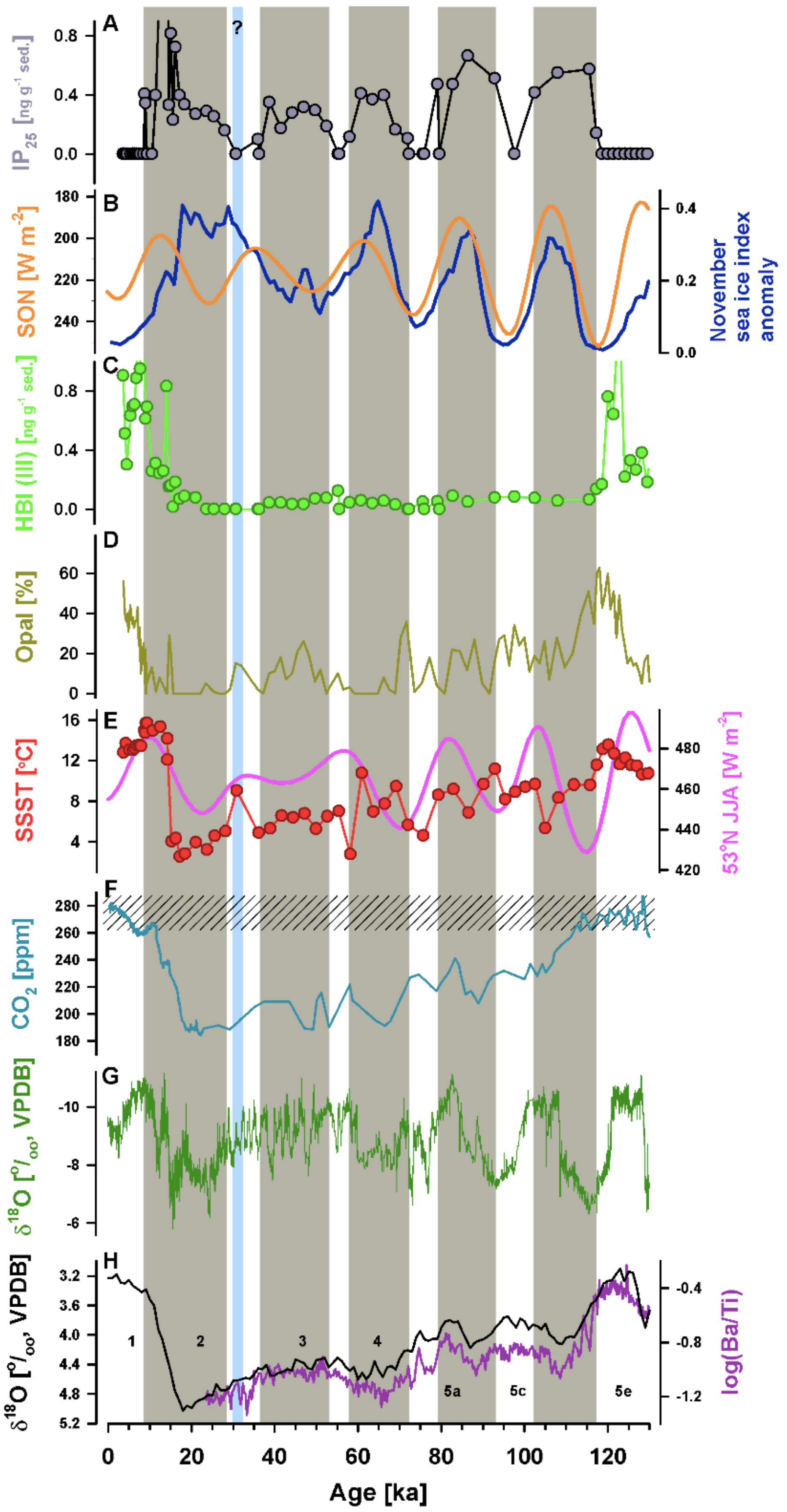

866
867

Figure 3

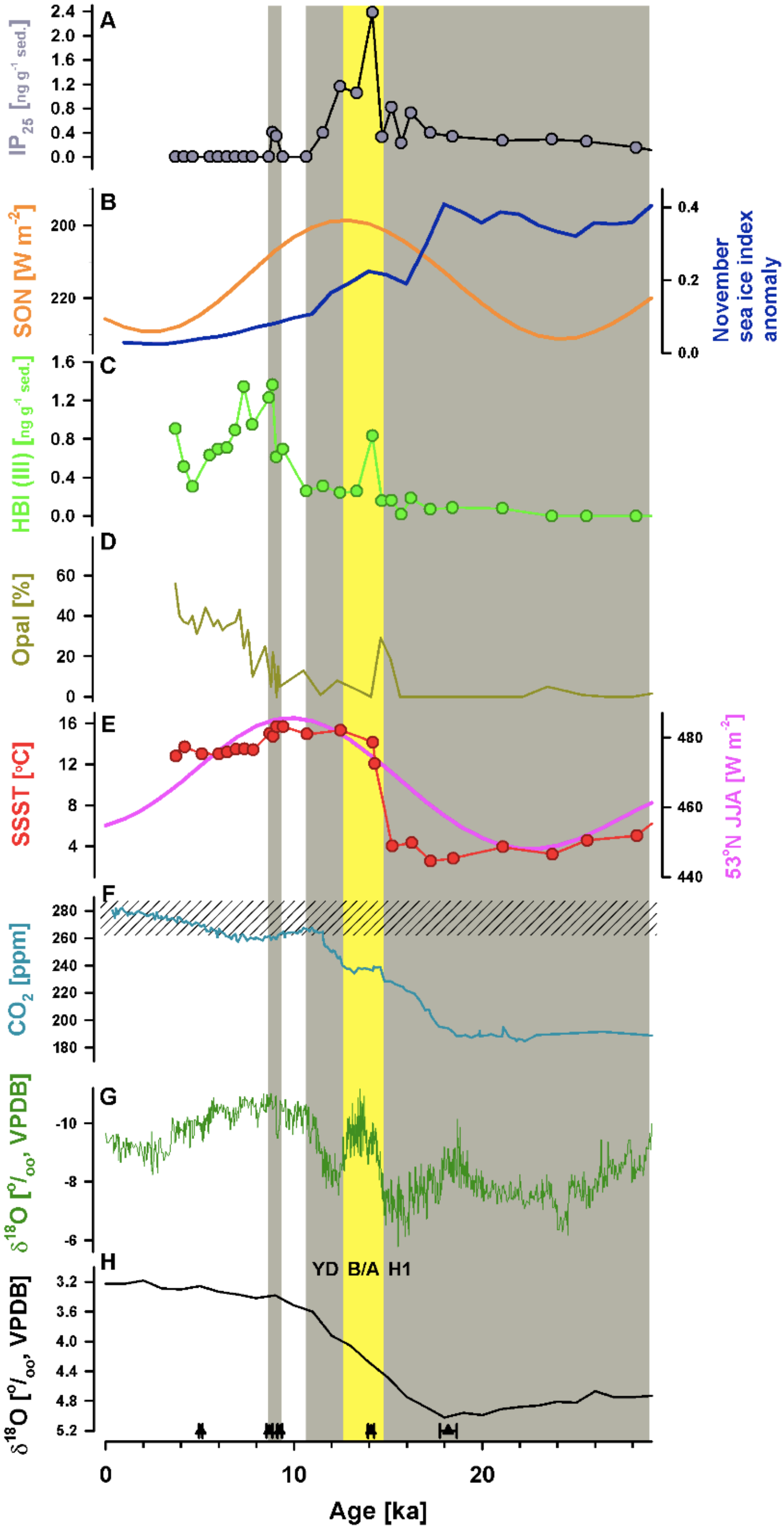

868
869 **Figure 4**

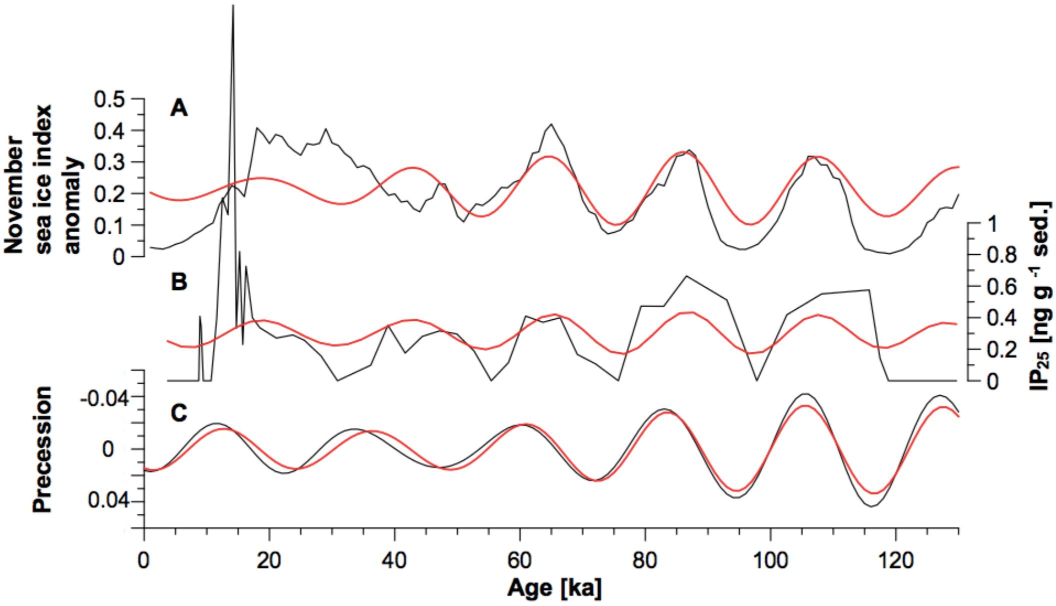
A
B
C
November sea ice index anomaly
0.5
0.4
0.3
0.2
0.1
0
1
0.8
0.6
0.4
0.2
0
IP25 [ng g -1 sed.]
Precession
-0.04
0
0.04
0
20
40
60
80
100
120
Age [ka]

Figure 5

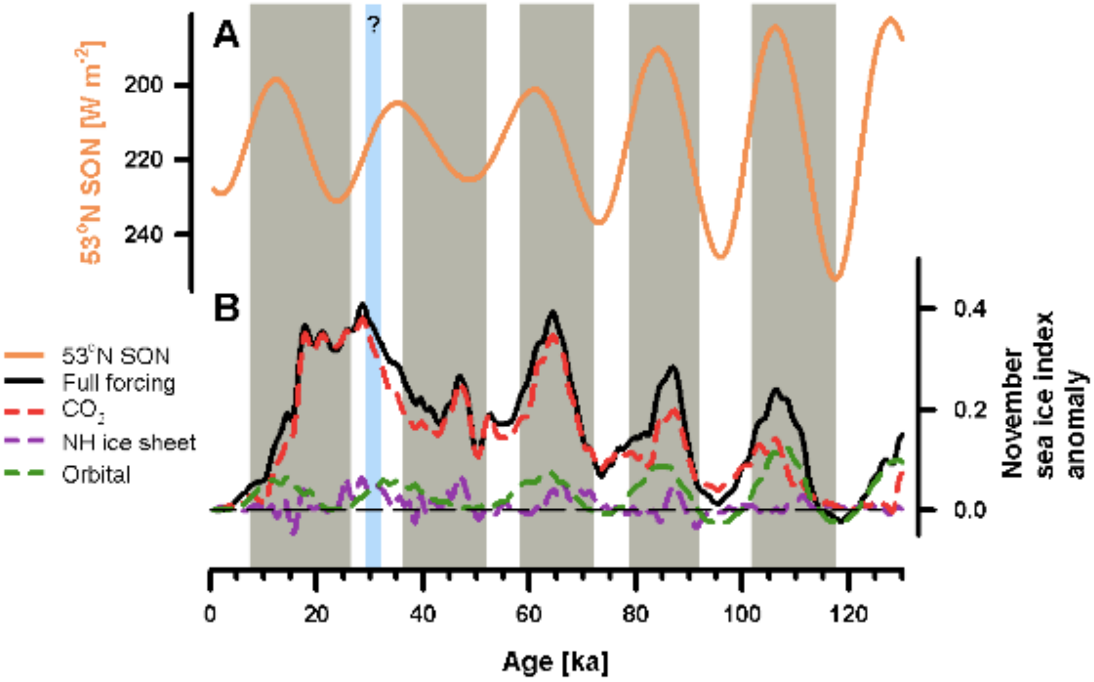
A
B
?
53°N SON [W m-2]
200
220
240
53°N SON
Full forcing
CO2
NH ice sheet
Orbital
November sea ice index anomaly
0.4
0.2
0.0
0
20
40
60
80
100
120
Age [ka]

Figure 6

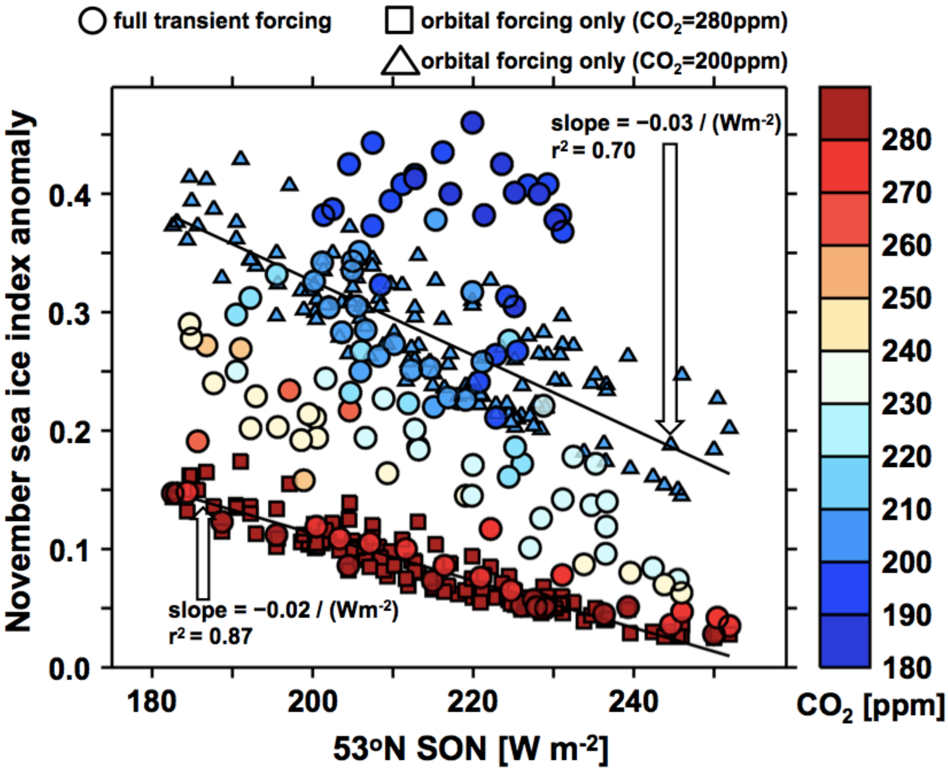
full transient forcing
orbital forcing only (CO_2=280ppm)
orbital forcing only (CO_2=200ppm)
slope = −0.03 / (Wm^{-2})
r^2 = 0.70
slope = −0.02 / (Wm^{-2})
r^2 = 0.87
November sea ice index anomaly
53°N SON [W m^{-2}]
CO_2 [ppm]
0.0
0.1
0.2
0.3
0.4
180
200
220
240
280
270
260
250
240
230
220
210
200
190
180

Figure 7

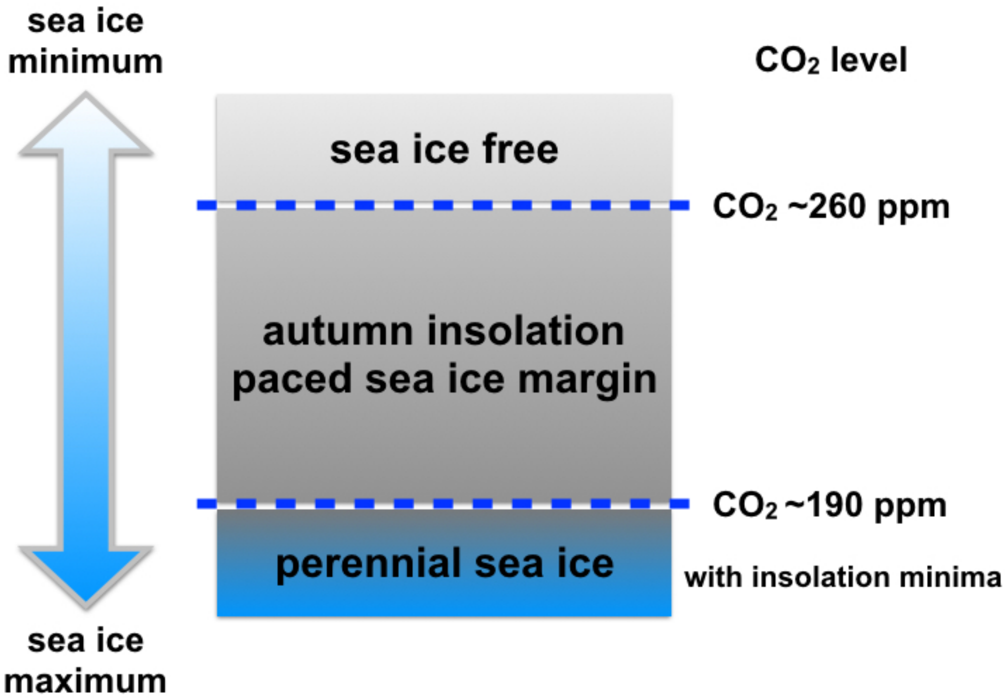

882
883 **Figure 8**
884

Supplementary Information

Lo et al., submitted

Atmospheric CO_2 control for precessional variability of sea ice in the Okhotsk Sea since 130,000 years ago

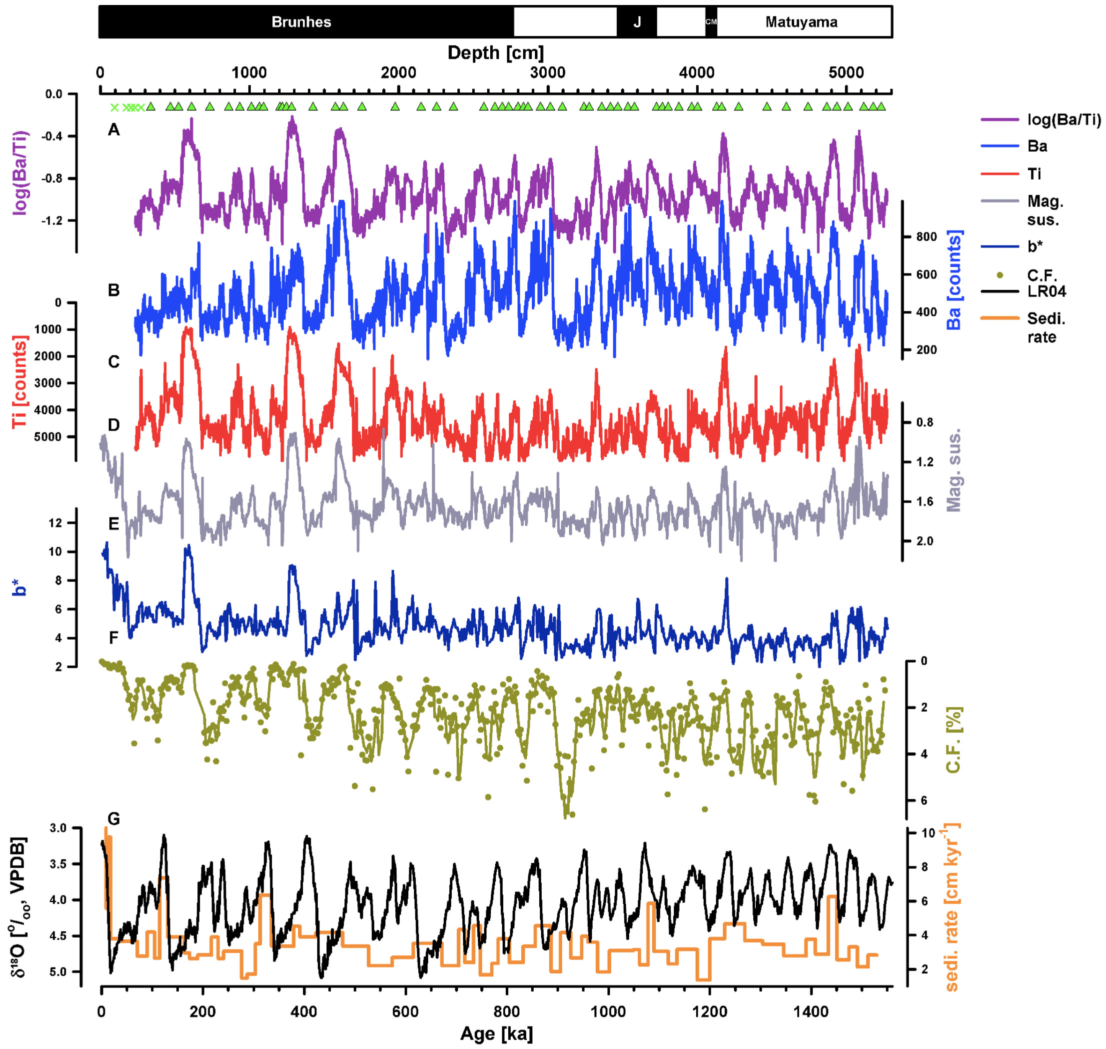

Supplementary Fig. 1. Age model of full sections of Site MD01-2414. (A) ITRAX scanned log(Ba/Ti) ratio, (B) Ba, (C) Ti, (D) magnetic susceptibility in log scale (Chou et al., 2011), (E) b* (Bassinot and Chen, 2002), (F) coarse fraction (C.F., this study) in weight percent (this study), and (G) global benthic composite oxygen isotope curve (black curve, Lisiecki and Raymo, 2005) and sedimentation rate (orange). Dark yellow line represents 3-point running average. Green crosses and triangles represent radiocarbon dates and age model tie points, respectively. Paleomagneitc epochs and reversal events in depth in the upper column. J and CM represent Jaramillo and Cobb Mountain, respectively (Chou et al., 2011).

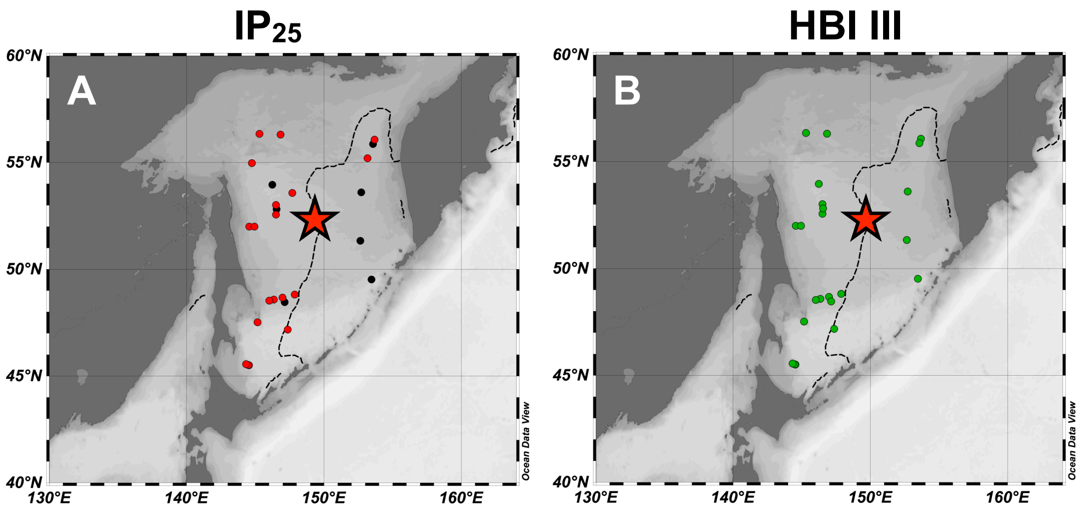

Supplementary Fig. 2. Surface sediments of IP_{25} and HBI III. Locations of core top samples and concentrations of (A) IP_{25} and (B) HBI III. Red and green dots are the samples with detected IP_{25} and HBI III, respectively. Black dots are samples in which IP_{25} is below detection limit. Note that data from Stoynova et al. (2013) are also included in this map. The map is made using Ocean Data Viewer (Schlitzer, 2017).

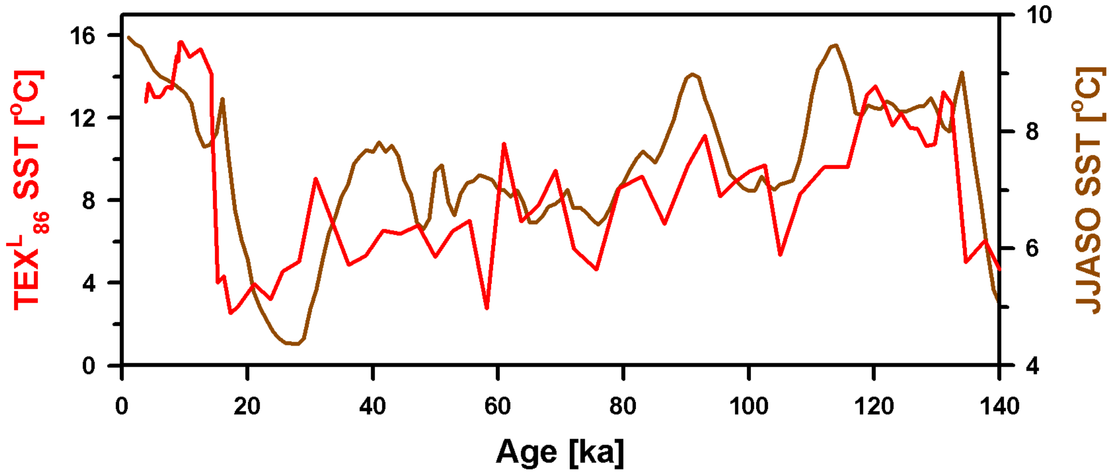

Supplementary Fig. 3. Comparisons between proxy-derived SSST and averaged monthly SST from simulations. TEX$^{L}_{86}$ derived SSST in the central Okhotsk Sea from Site MD01-2414 in red and June-July-August-September-October (JJASO) averaged SST from this study in brown.

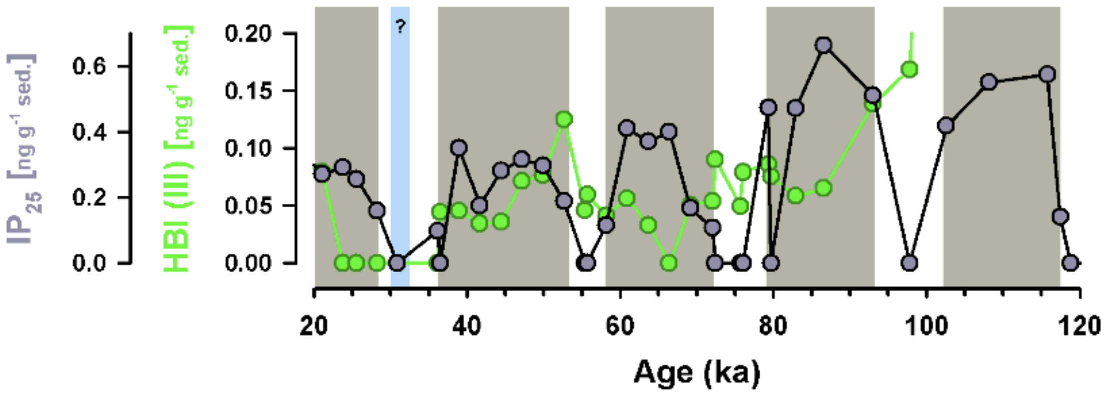

Supplementary Fig. 4. MD01-2414 IP_{25} and HBI III concentrations during 120-20 ka. IP_{25} and HBI III concentrations are in gray and green, respectively. Background shading is the same as Fig. 3.

Supplementary Table 1. AMS ^{14}C dates of MD01-2414. Planktonic foraminiferal (*Neogloboquadrina pachyderma*, *sinistral*, > 125 µm) AMS ^{14}C dates results of Site MD01-2414. Calendar ages were calculated by using CALIB 7.1 software (Reimer et al., 2013) with a reservoir age ΔR = 450 ± 90 years.

Sample code	Corrected depth (cm)	Conventional ^{14}C age (ka)	Error (kyr, 1σ)	Calendar age (ka)	Error (kyr, 1σ)
QAS3260	33	5.23	0.05	5.06	0.10
QAS3261	113	8.63	0.10	8.70	0.16
QAS3262	143	9.04	0.10	9.26	0.12
QAS3263	170	13.06	0.09	14.10	0.16
QAS3264	210	15.83	0.41	18.20	0.46

Supplementary Table 2. Phase relationships between proxy data, transient model simulations and insolation/precession. Phase relationships between precession JJA (averaged June, July, August) insolation, SON (averaged September, October, November) insolation (Laskar et al., 2004), organic geochemical proxies (IP_{25}, and SSST) and transient model results, given in kyr. The cross Blackman-Tukey method of AnalySeries (Paillard et al., 1996) was used with a Bartlett window. Positive phase indicates a lag of proxies relative to precession/insolation here. Note that autumn insolation lags precession. Obliquity is not analyzed because of the rather short time period of the record.

	Precession	JJA 53°N	SON 53°N
IP_{25}	5.7 ± 1.5	-6.1 ± 1.5	7.5 ± 1.6
SSST	-8.9 ± 2.2	0.1± 1.9	-7.5 ± 2.1
November sea ice index anomaly	-2.4 ± 0.4	-4.1 ± 0.6	9.0 ± 0.6

Supplementary Table 3. Surface sediments locations, IP_{25}, and HBI III concentrations.

Station	Lat. (ºN)	Long. (ºE)	IP_{25} (ng g^{-1} sed.)	HBI III (ng g^{-1} sed.)
55-9-1	49.52	153.45	0	3.8
55-11-2	51.33	152.65	0	9.5
55-13-2	53.61	152.72	0	113.3
55-14-2	56.08	153.68	0.9	3.5
55-15-2	55.86	153.56	0	31.6
55-17-2	56.31	146.84	0.7	14.3
55-18-2	56.34	145.31	2.2	47.5
55-19-2	53.96	146.24	0	0.2
55-23-2	53.01	146.51	0.4	0.2
55-24-2	52.81	146.55	0	0.3
55-25-2	52.56	146.51	1.0	1.1
55-27-2	52.00	144.56	4.4	5.5
55-30-1	52.00	144.94	15.7	81.9
55-34-2	48.82	147.87	1.1	3.4
55-35-2	48.53	146.02	0.8	0.8
55-36-2	48.58	146.36	2.4	6.3
55-38-2	48.68	146.98	1.7	7.1
55-41-2	48.46	147.14	0	0.4
55-43-2	47.18	147.36	2.2	3.5
55-44-2	47.52	145.16	2.4	3.6
44-46-2	45.51	144.54	2.2	7.4
55-47-2	45.52	144.48	3.0	19.6
55-48-2	45.55	144.33	6.5	29.9

Supplementary Data Table. Site MD01-2414 XRF scanning, coarse fraction, IP_{25} and HBI III concentrations, TEX^{L}_{86} derived SSST data. November sea ice index anomaly and sensitivity run data are also included.

References

Bassinot, F., Chen, M.-T., 2002. Physical properties of sediment core MD01-2414. doi:10.1594/PANGAEA.80047.

Chou, Y.-M., Lee, T.-Q., Song, S.-R., Chen, K.-J., 2011. Magnetostratigraphy of marine sediment core MD01-2414 from Okhotsk Sea and its paleoenvironmental implications. Mar. Geol. 284, 149-157.

Laskar, J., Robutel, P., Joutel, F., Gastineau, M., Correia, A.C.M., Levard, B., 2004. A long-term numerical solution for the insolation quantities of the Earth. Astron. Astrophys. 428, 261-285.

Lisiecki, L.E., Raymo, M.E., 2005. A Pliocene-Pleistocene stack of 57 globally distributed benthic $\delta^{18}O$ records. Paleoceanography 20, PA1003.

Paillard, D., Labeyrie, L., Yiou, P., 1996. Macintosh program performs time-series analysis, EOS Trans. 77, 379.

Reimer, P. J., Bard, E., Bayliss, A., Beck, J. W., Blackwell, P. G., Bronk Ramsey, C., Buck, C. E., Cheng, H., Edwards, R. L., Friedrich, M., Grootes, P. M., Guilderson, T. P., Haflidason, H., Hajdas, I., Hatté, C., Heaton, T. J., Hoffmann, D. L., Hogg, A. G., Hughen, K. A., Kaiser, K. F., Kromer, B., Manning, S. W., Niu, M., Reimer, R. W., Richards, D. A., Scott, E. M., Southon, J. R., Staff, R. A., Turney, C. S. M., and van der Plicht, J., 2013. IntCal13 and Marine13 radiocarbon age calibration curves 0–50,000 years cal BP. Radiocarbon, 55(4),1869–1887, https://doi.org/10.2458/azu_js_rc.55.16947, 2013.

Schlitzer, R., 2017. Ocean Data View, odv.awi.de.

Stoynova, V., Shanahan, T.M., Hughen, K.A., de Vernal, A., 2013. Insights into Circum-Arctic sea ice variability from molecular geochemistry. Quat. Sci. Rev. 79, 63-73.